

Provided for non-commercial research and education use.
Not for reproduction, distribution or commercial use.



This article appeared in a journal published by Elsevier. The attached copy is furnished to the author for internal non-commercial research and education use, including for instruction at the authors institution and sharing with colleagues.

Other uses, including reproduction and distribution, or selling or licensing copies, or posting to personal, institutional or third party websites are prohibited.

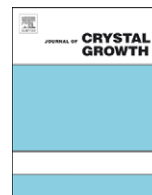
In most cases authors are permitted to post their version of the article (e.g. in Word or Tex form) to their personal website or institutional repository. Authors requiring further information regarding Elsevier's archiving and manuscript policies are encouraged to visit:

<http://www.elsevier.com/copyright>



Contents lists available at ScienceDirect

Journal of Crystal Growth

journal homepage: www.elsevier.com/locate/jcrysgro

Characterization of detector-grade CdZnTe crystals grown by traveling heater method (THM)

S.A. Awadalla^{a,*}, J. Mackenzie^a, H. Chen^a, B. Redden^a, G. Bindley^a, M.C. Duff^b, A. Burger^c, M. Groza^c, V. Buliga^c, J.P. Bradley^d, Z.R. Dai^d, N. Teslich^d, D.R. Black^e

^a Redlen Technologies, Sidney, B.C., Canada V8L 5Y8

^b Savannah River National Laboratory, Aiken, SC 29808, USA

^c Fisk University, Nashville, TN 37208-3051, USA

^d Lawrence Livermore National Laboratory, Livermore, CA 94550, USA

^e National Institute of Standards and Technology, Gaithersburg, MD 20899, USA

ARTICLE INFO

Article history:

Received 15 May 2009

Received in revised form

30 October 2009

Accepted 3 November 2009

Communicated by Dr. R. James

Available online 20 November 2009

Keywords:

A1. CZT

A2. THM

A2. Secondary phases

A3. Surface treatment

ABSTRACT

This work focuses on the 3. Results and discussion characterization of $10 \times 10 \times 10 \text{ mm}^3$ THM-grown CdZnTe detector-grade crystals that have been post-growth annealed to remove the secondary phases (SPs). All three detectors showed an average energy resolution of $\sim 1.63\%$ for a small guarded pixel with 3.5 mm diameter, measured using ^{137}Cs —662 keV with an average peak-to-Compton ratio of 2.7. The characterization showed vestiges of SPs and micro-twins present in some of the crystals indicating that the SPs prior to annealing were large and had size in the range of 100–500 μm . The various detectable structural features, such as micron twins, strains and sub-micron level of Te inclusions seemed to have little or no influence in the radiation spectrometer performance of the detectors; this is possibly because they are either having low density or electrically inactive.

© 2009 Elsevier B.V. All rights reserved.

1. Introduction

$\text{Cd}_{1-x}\text{Zn}_x\text{Te}$ or “CZT” crystals continue to be the material of choice for room temperature-based detection of γ radiation. However, the radiation detection properties of CZT crystals vary widely. These variances are not completely understood. They have been attributed to a combination of factors such as point defects, structural and morphological heterogeneities within the crystals, such as twinning, pipes, grain boundaries (polycrystallinity) and secondary phases (SP) [1–5]. During the past 15 years of CZT development, considerable improvements have been made. As the size of useful detectors gradually increased from a few mm^3 to a few cm^3 , the limiting factor in the detector performance seemed to vary from carrier trapping by point defects, pipes and cracks to what has more recently been named in the literature as either Te inclusions [as recently described by Carini et al. (2006), Bolotnikov et al. (2007) and Refs. therein] or as Te precipitates [6–8]. An explanation for the formation of these Te-rich phases is due to the presence of excess Te in the melt of CZT phases. Even if the starting charge is stoichiometric or slightly Cd-rich, elemental Cd, which is the most volatile species, will preferentially evaporate

into the free space of the ampoule and leave behind a Te-rich melt. Tellurium-rich phases are thought to form during crystal growth due to the retrograde solubility within the phase diagram [9,10]. Such phases were noted by Rai et al. (1996) when they observed the presence of many $< 0.1 \mu\text{m}$ sized Te-rich SP (called precipitates) in CdTe crystals [11].

One of the early improvements in the CZT technology addressed the issue of the cracks and the voids within pipes. In recent years these performance limiting features have almost been eliminated from the boules grown with current methods. Fortunately, crystals made using low pressure vertical Bridgman (e.g., MVB by Yinnel Tech in the USA) [12] and traveling heater method (THM) (e.g., by Redlen in Canada) [13,14] growth processes provide good control of the growth, and these methods produce large single crystals. This work discusses the characterization of $10 \times 10 \times 10 \text{ mm}^3$ CZT crystals grown using THM.

2. CZT crystal growth and selection

Three thick samples, MC34-66, MC25-39 and C640-39, were selected and sent to SRNL for characterization. All samples were processed under the same annealing conditions. MC34-66 and MC25-39 have similar crystal growth conditions and furnace

* Corresponding author.

E-mail address: salah.awadalla@redlen.com (S.A. Awadalla).

design, while C640-39 was grown using a modified growth and cooling method. The crystals were grown by modified THM, and wafers experienced customized post-growth annealing. The thickness of the sliced wafers was increased from 6 to 12 mm allowing the production of 10-mm-thick detectors. Both growth and annealing parameters were modified to produce thicker wafers having lower structural and intrinsic defect density. The post-annealed wafers from the modified processes were then analyzed using IR transmission microscopy to evaluate the remaining Te inclusions.

3. Device fabrication, characterization and testing

3.1. Current–voltage (*I*–*V*) measurement

All three crystals were fabricated as-polished (i.e., no chemical etching) with one 3.5 mm diameter guarded pixel with pixel to guard ring distance of 0.3 mm. The current–voltage (*I*–*V*) measurement is used to extract the resistivity of the samples and check the contact's Ohmicity. *I*–*V* curves were obtained using the Keithley 237 Power Unit assisted by a PC computer using the ICS (Interactive characterization software) software of Metrics Technology, Inc. The obtained *I*–*V* curves are shown in Fig. 1. As seen in the figures, all three samples showed low dark leakage current indicating high resistivity and good Ohmicity. All three samples showed different amounts of residual dark current at 0 V applied bias. The reason is unknown; however the calibration of the *I*–*V* system could be the cause. In addition, from the extracted resistivity, one can see that THM grown material is semi-insulating. The semi-insulating nature of these crystals is obtained through compensating residual Cd vacancies during growth using doping and by post-growth annealing in Cd vapor.

3.2. Device performance

The detector performance of the three crystals was tested with a 2 μCi ^{137}Cs source using Canberra MCA model multiport II driven by Genie 2000, version 2.1. Fig. 2a–c shows the ^{137}Cs 662 keV responses of the detectors. All of the detectors were biased to 1600 V applied bias; MC34-66 and C640-39 gave 1.5% and 1.6% FWHM, respectively, with 900 s live time and 0.5 μs shaping time, while MC25-39 gave a 1.8% FWHM with 600 V and 1.0 μs shaping time. Recall that MC25-39 and MC34-66 were grown and post-growth annealed under the same conditions, yet the MC34-66 photo peak collected with a shorter shaping time

and higher energy level indicating a better charge collection efficiency of MC34.

3.3. Infrared (IR) microscopy

IR transmission microscopy had been known to be one of the most effective ways of detecting Te inclusions, precipitates, and other Te decorated structural defects in CZT. Unpolarized IR light was used to look for cracks, grain boundaries and other major defects as shown in Fig. 3a–c. Sample MC34-66 possesses a twin boundary. Sample MC25-39 and C640-W39 are relatively defect-free. Cross polarized IR light topography was used to detect internal stress due to the growth and the post-growth treatments of CZT crystals. Fig. 4a–c shows the differences among the three samples. Sample MC34-66 showed high striations among the three crystals indicating higher strain level. IR (unpolarized) microscopic imaging was used to detect the presence of SP, their size and their distribution. Fig. 5a–c shows the differences. For all 3 samples there were only a few clusters of SP that were detectable by IR (e.g., those with a size $> 1 \mu\text{m}$), and information about their size and density distribution were not estimated.

3.4. X-ray topography

X-ray topography (XRT) was performed at the Advanced Photon Source at Argonne National Laboratory (Argonne, IL) using beam line 33-BM. An incident energy of 9 keV was selected from the white radiation source using a double crystal monochromator with Si(111) crystals. A rotating foam disc located between the sample and monochromator functioned as a random phase object to remove the structure in the incident beam due to phase contrast resulting from imperfections in the beam line Be windows. For these measurements, the sample faces were parallel to the (111) orientation, and symmetric (333) images were recorded from these faces. The film was positioned parallel to the sample surface, so that the recorded images would not have any foreshortening. Images were recorded on a high contrast lithographic film, and for all images the diffraction vector points out of the image.

X-ray topographic images of the three CZT crystals are shown in Fig. 6a–d. Large angular variation (inferior quality) exists in MC34-66 (Fig. 6a) relative to that of MC25-39 crystal (shown in Fig. 6d) indicating higher degree of strain. The degree of strain is best demonstrated by not only the number of exposures required to record the diffraction-based image of the 1 cm³ crystal but the

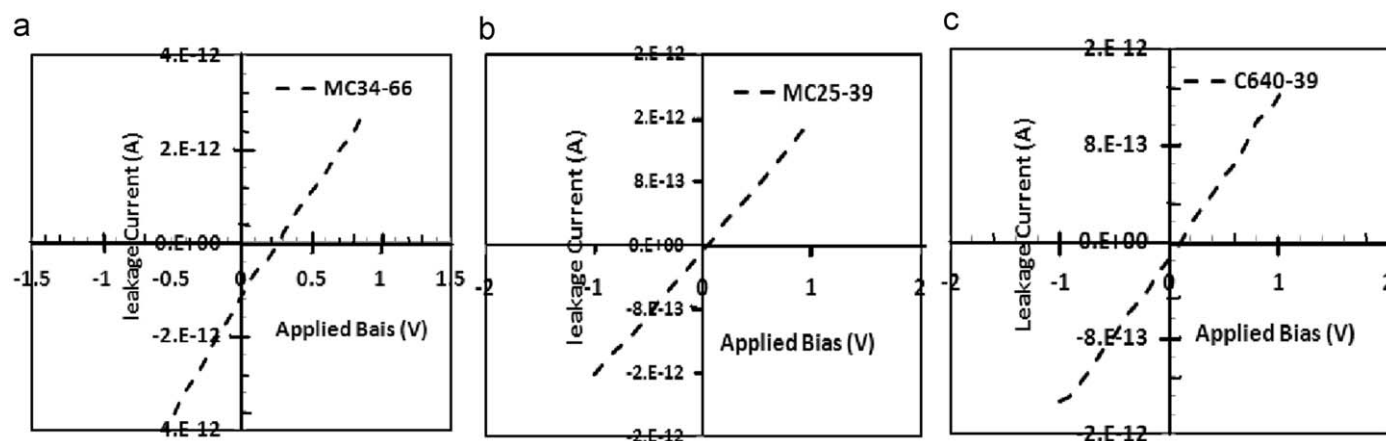


Fig. 1. Current–voltage characteristics for (a) MC34-66, $\rho_V = 2 \times 10^{10} \Omega \text{ cm}$; (b) MC25-39, $\rho_V = 6 \times 10^{10} \Omega \text{ cm}$; and (c) C640-39, $\rho_V = 7.3 \times 10^{10} \Omega \text{ cm}$.

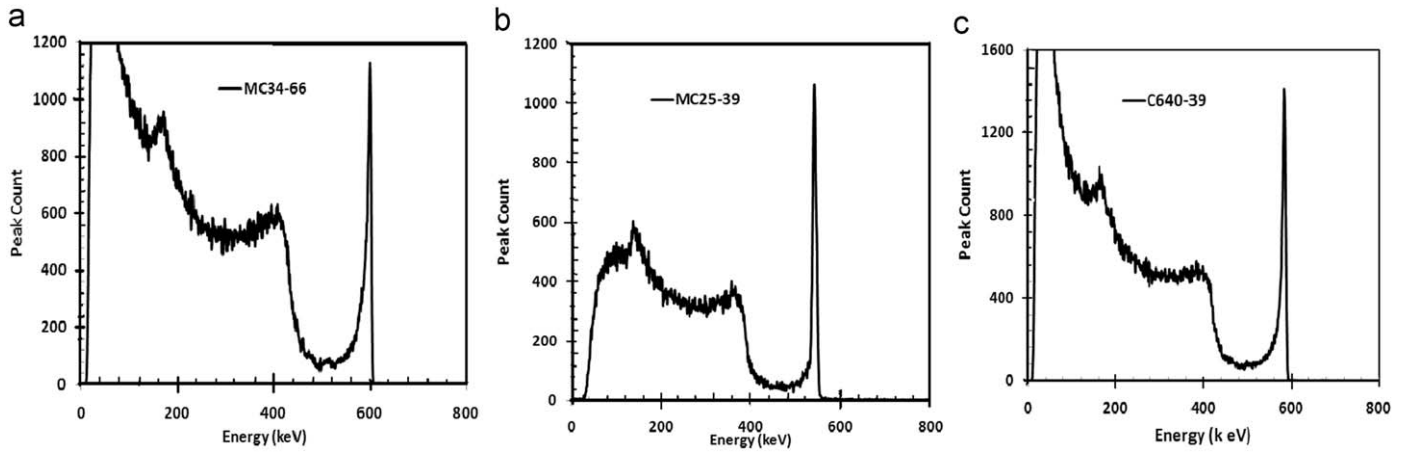


Fig. 2. Detector testing of THM-CZT showing a ^{137}Cs energy spectrum for (a) RMC34-66 with an energy resolution for 662 keV of 1.5% and peak/Compton ratio 1.9; (b) MC25-39 with an energy resolution for 662 keV of 1.8% and peak/Compton ratio 2.9; and (c) C640-39 with an energy resolution for 662 keV of 1.6% and peak/Compton ratio 2.6.

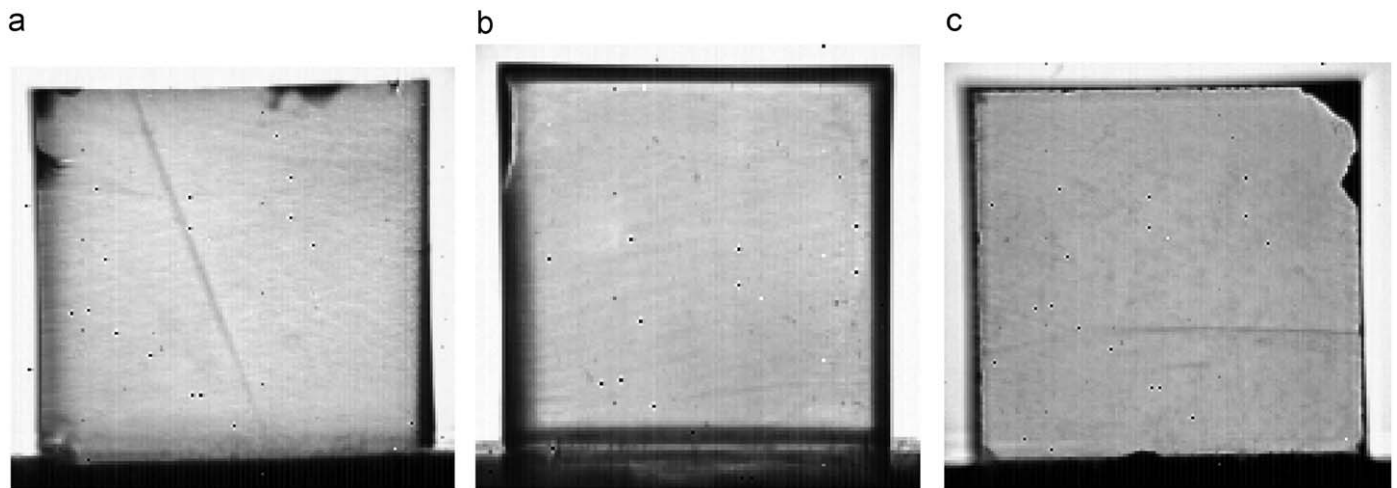


Fig. 3. IR transmission images of, with 100-mm² field of view, unpolarized light of THM-CZT: (a) MC34-66, (b) MC25-39, and (c) C640-39.

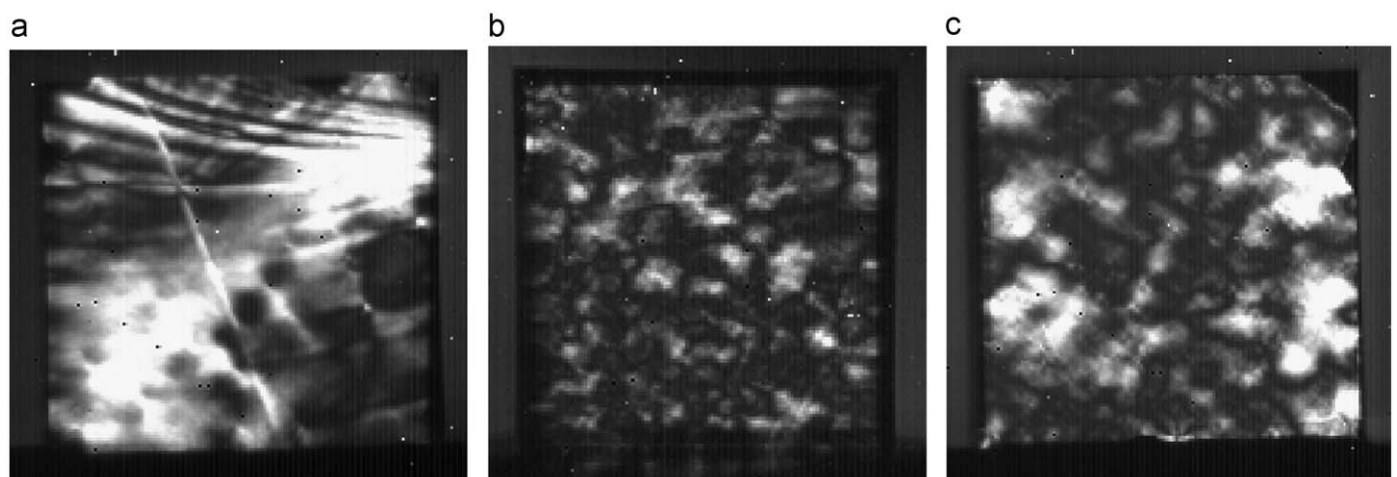


Fig. 4. Cross polarized IR transmission images, with 100-mm² field of view ($\lambda=1150$ nm) of THM-CZT. Sample ID: (a) MC34-66, (b) MC25-39, and (c) C640-39.

degrees of rotation required to make the multi-exposure image resolved on the film. The amount of strain present in MC34-66 (5 exposures with 0.20° angles of rotation between each exposure) is considerably greater than that of MC25-39

(6 exposures with 0.03° angles of rotation between each exposure). In contrast, sample C604-39 (Fig. 6c) required one exposure to create a suitable image, which indicates that this crystal is not as strained as the other two crystals.

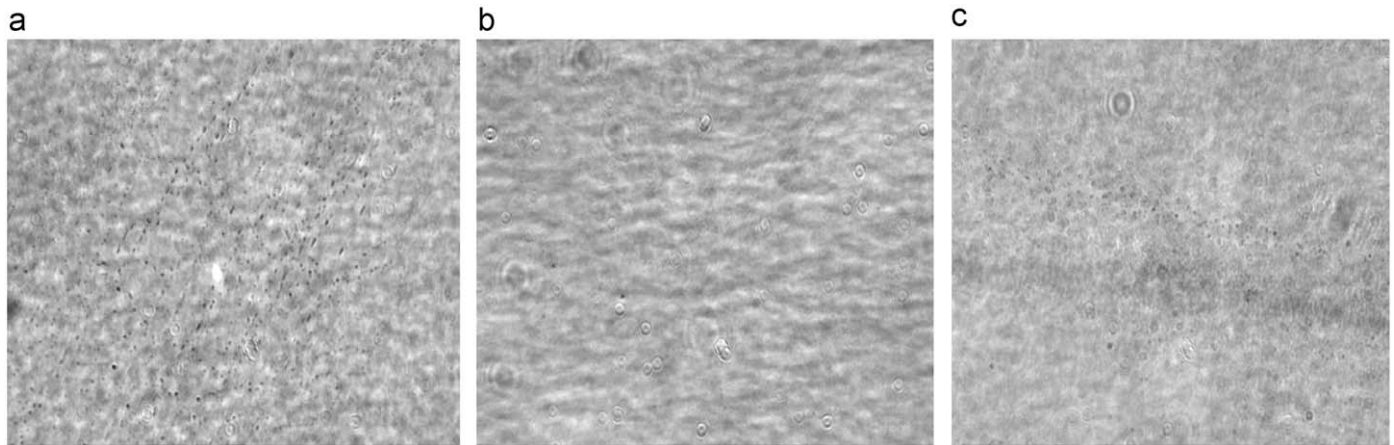


Fig. 5. IR microscopic imaging of internal detail ($1.75 \times 1.3 \text{ mm}^2$, depth of field $\sim 0.4 \text{ mm}$) of (a) MC34-66, (b) MC25-39, and (c) C640-39. $100 \mu\text{m}$.

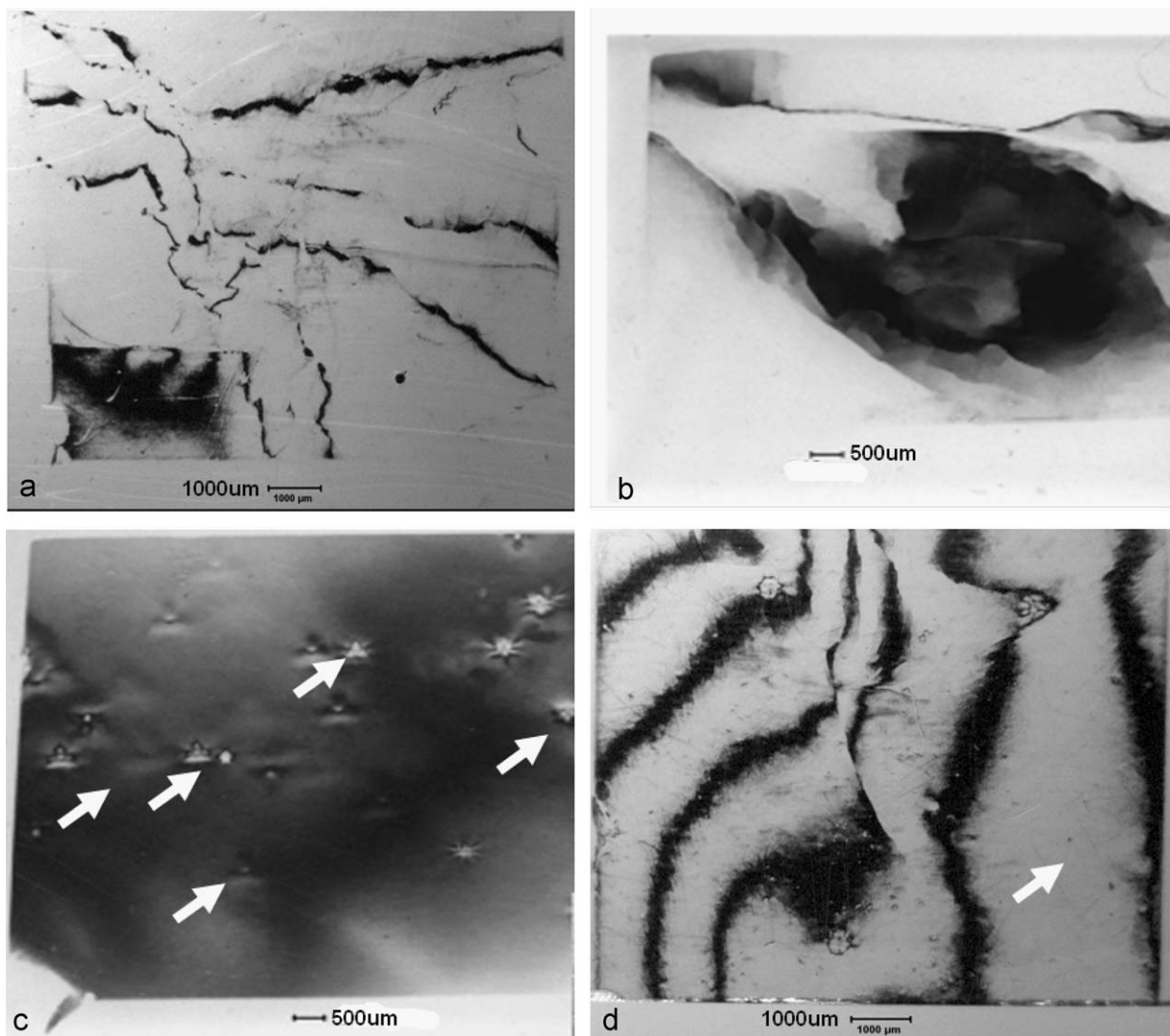


Fig. 6. X-ray topographs (all 333 symmetric images) of two different faces of MC34-66 as shown in (a) and (b); (c) sample C640-39; and (d) an X-ray topograph of MC25-39. White arrows denote areas with vestiges of large triangular-shaped SP (in c) and large hexagonal-shaped secondary phases (in d). Note that the density of these feature is about $0.5 - 3 \times 10^2 \text{ incl/cm}^2$.

In addition, Fig. 6 shows vestiges of triangular and hexagonal-shaped inclusion which are not different in any way because inclusions are trapped droplets of solvent. The saturation level of

the trapped solvent is a likely control on the shape of the inclusion. In $\langle 111 \rangle$ oriented growth, the trapped inclusion is initially triangular but when the crystal cools, oversaturated

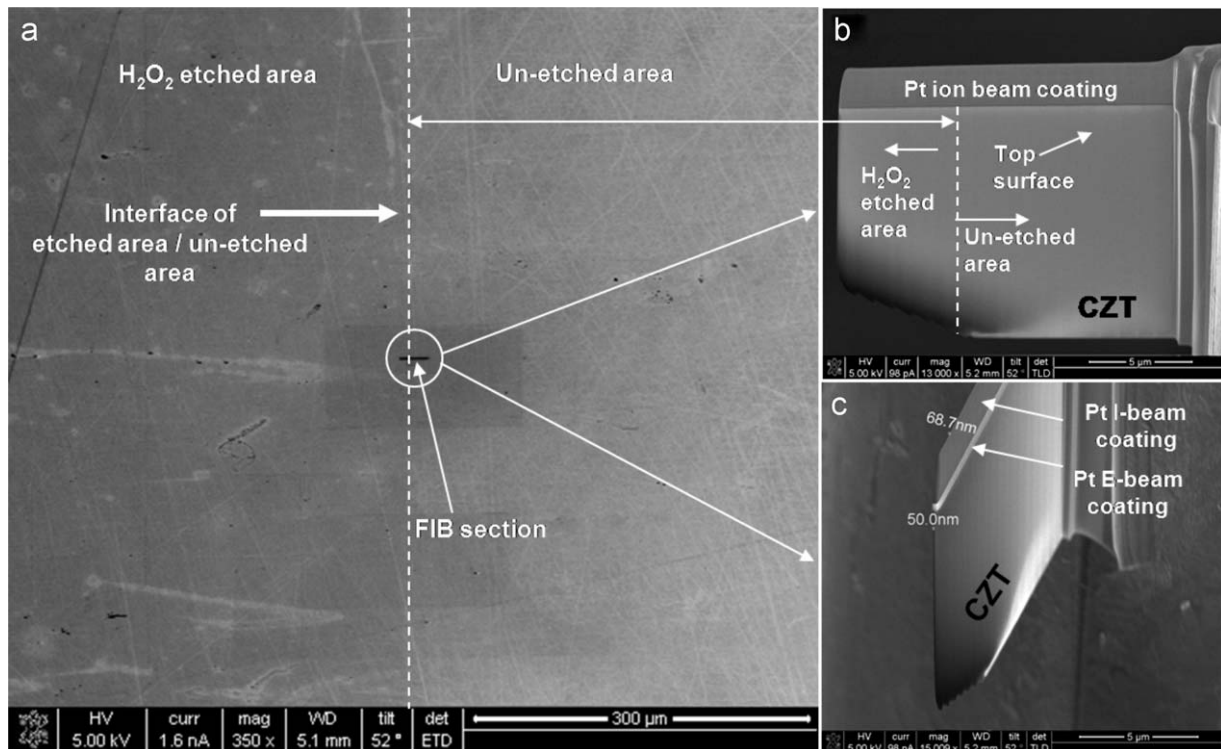


Fig. 7. SEM images of (a) peroxide treated and untreated regions on MC25-39 with images (b) and (c) showing two views of a thin section (removed by focused ion-beam milling) from the region delineated in the circle as shown in (a).

inclusions will precipitate CZT at the corners, effectively infilling them and generating a final hexagonal inclusion shape. Due to the changing saturation states of the solvent during crystallization, both saturated and oversaturated drops are trapped yielding triangular and hexagonal shapes. The size and distribution of these features match SP phases observed in IR but is not confirmed explicitly.

As mentioned before, the examination of MC34-66 with cross polarized IR light (Fig. 4a) revealed higher striations that were not present in the other two CZT crystals (Fig. 4b–c). The striations in MC34-66 may be associated with the high degree of crystal strain that is detected in the topography studies of MC34-66. The origin of these striations is unknown since the other crystal grown under the same growth conditions and furnace design in $\langle 111 \rangle$ direction did not suffer from the same amount of striations.

In addition, large heterogeneities (100–400 μm) of what resemble SP are detected in materials C640-39 and MC25-39 (in Fig. 5c and d). However, in general, these particularly large features were not detected with transmission IR imaging (Fig. 4a–c) because the post-growth annealing process removes these SP features. So, it is considered that the features in the XRT images are “vestiges” of SP prior to post-growth annealing. These vestiges are only apparent in the topography because the annealing process does not remove the crystalline strain (deformation) that was associated with the SP prior to their removal by annealing.

4. SEM and TEM analysis

To learn more about the CZT properties and their structural defects, half of sample MC25-W39 was exposed to concentrated, 31.9% hydrogen peroxide (a passivating agent) for 5 min, and the other half was left untreated. The treated sample was sent to LLNL for examination by SEM using an FEI Nova 600 Nanolab

Dual-beam focused ion beam scanning electron microscope (FIB-SEM). SEM analysis, shown in Fig. 6, showed no presence of faceted SP, such as those found with detector-grade CZT made by modified vertical Bridgman (MVB) growth methods at Ynnel Tech [18]. Additionally, the SP or any evidence of their vestiges were not apparent on the THM grown CZT crystal based on SEM imaging—in contrast to the XRT studies. In general, SEM studies revealed that the untreated side of the crystal was considerably homogeneous.

CZT treatment with H_2O_2 is thought to result in the formation of a high resistivity coating of CdTeO, according to phase diagram predictions [22]. The STEM-EDS analysis indicates that the peroxide treatment did not significantly change the Cd:Te composition of the CdZnTe surface, which is consistent with but not conclusive that a CdTeO phase has not formed on the surface. Fig. 8a–e of MC25-39 shows no detectable difference of composition between the H_2O_2 -immersed region of the top surface (area 4) and un-immersed region (area 3). However, the atomic ratio of Cd/Te on top surface (areas 3 and 4) is slightly lower ($\sim 5\%$ lower) than that of the CZT bulk (area 2). SEM imaging studies (Fig. 7) of MC25-39 reveal visual differences between the H_2O_2 -treated surface and the untreated surface—indicating that the surface properties were altered by H_2O_2 contact. A closer examination of a thin section made of the treated surface was performed using focused ion beam to remove an electron-thin sample for TEM analyses that contained regions with both treatments (immersed and not immersed), in addition to some intact subsurface material (a few μm deep) as mentioned previously (Fig. 8).

To be thorough, a thin section of SP-based area of interest was prepared by ion-beam milling for high resolution-transmission electron microscopy (HR-TEM) studies. HR-TEM studies were performed with a 200 keV FEI Technai20 G2 FEG monochromated scanning transmission electron microscope (STEM) with high

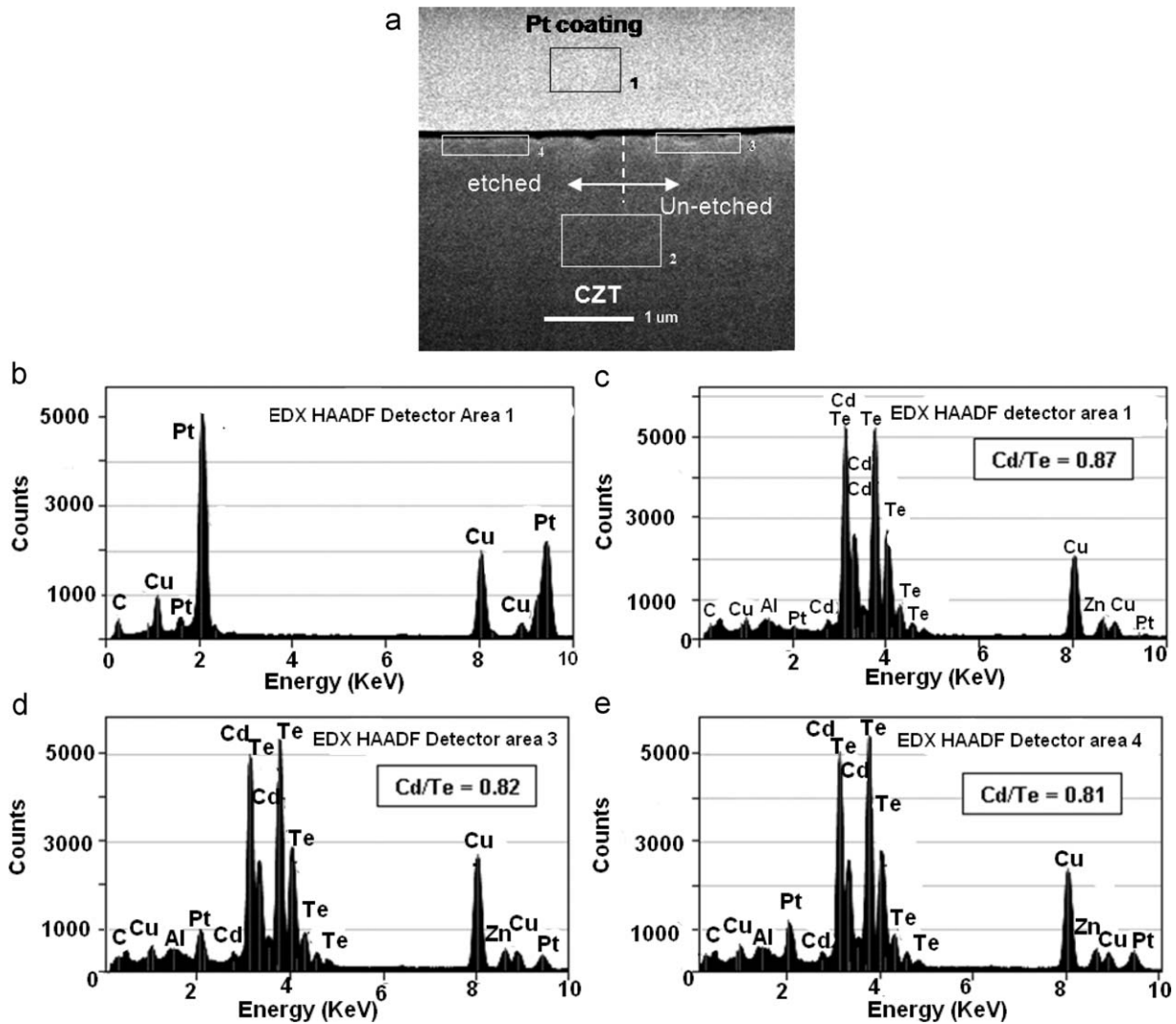


Fig. 8. STEM HAADF image of (a) peroxide treated and untreated regions on MC25-39 with energy dispersive spectra for (b) the Pt coated sample, (c) the bulk material, (d) the un-etched material and (e) the peroxide etched material. Note that the origin of a large Cu signal is known; we believe of the possibility of interference between Cu and Zn and the signal could possibly be a Zn signal.

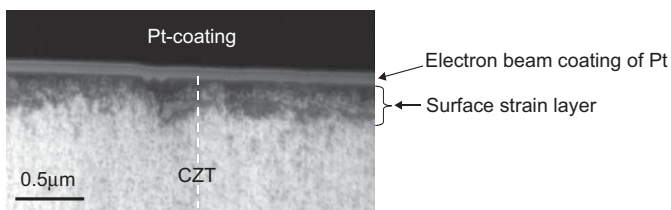


Fig. 9. Bright field TEM image of peroxide treated region (left half of image) and untreated (right half) region on MC25-39.

angle annular dark field (HAADF) detector with a Si(Li) solid state X-ray detector (0.3 steradians solid angle). TEM bright-field imaging of the top surface of MC25-39 is shown in Fig. 9.

It appears that the surface on the etched side is smoother, indicating the removal of the surface irregularity and the passivation of the dangling bonds that result in polished-like surface, than that on un-etched side. In addition, there is a strain layer with a thickness of 0.25–1.5 μm below the top surface—regardless of treatment. This strain may be introduced during cutting and/or polishing. In general, we could not detect any effect of the peroxide treatment. This suggests that the oxidizing effect of the treatment remains close to the surface, which is consistent

with observations by Bartlett (1996) who observed a surface oxidation layer thickness of a few tens of nm [19].

5. Conclusion

Despite the differences in the amount of defect levels, all three detectors showed good energy resolution. Vestiges of SP that were detected in these materials indicate that the SP prior to annealing was large and had a range in size (based on topographic imaging) of 100–500 μm. Sample MC34-66 is a high performance material (based on its %FWHM for an energy of 662 keV) but relative to the two other THM materials that we examined, it had a high amount of stress, crystalline strain, and considerably more SP that were visible with FTIR imaging (but not with XRT imaging). MC34-66 also has defects such as a twin boundary that is fairly evident in comparison to the features that were identified in the characterization of the other two THM grown Redlen samples. These various detectable structural features seem to have little or no influence in the radiation spectrometer performance of the detector possibly either because they have low density; detector geometry is much larger than the spatial scale of the features and/or electrically inactive.

Acknowledgments

This work was supported by the US DOE—National Nuclear Security Administration through the Office of Nonproliferation Research and Development—NA-22 and National Science Foundation through the Fisk University Center for Physics and Chemistry of Materials (CPCoM), Cooperative Agreement CA: HRD-0420516 (CREST program), and through the US DOE NA-22 Grant no. DE-FG52-05NA27035. Use of the Advanced Photon Source was supported by the U. S. Department of Energy, Office of Science, Office of Basic Energy Sciences under Contract no. DE-AC02-06CH11357.

References

- [1] J.R. Heffelfinger, D.L. Medlin, R.B. James, *MRS Symp. Proc.* 487 (1998) 33.
- [2] M. Schieber, T.E. Schlesinger, R.B. James, H. Hermon, H. Yoon, M. Goorsky, *J. Cryst. Growth* 237–239 (2002) 2082.
- [3] C. Szeles, M.C. Driver, *SPIE Proc.* 3446 (1998) 1.
- [4] C. Szeles, S.E. Cameron, J.-O. Ndap, W.C. Chalmers, *IEEE Trans. Nucl. Sci.* 49 (2002) 2535.
- [5] J. Shen, D.K. Aidun, L. Regel, W.R. Wilcox, *J. Cryst. Growth* 132 (1993) 250.
- [6] G.A. Carini, A.E. Bolotnikov, G.S. Camarda, G.W. Wright, L. Li, R.B. James, *Appl. Phys. Lett.* 88 (2006) 143515.
- [7] A.E. Bolotnikov, G.S. Camarda, G.A. Carini, Y. Cui, L. Li, R.B. James, *Nucl. Instrum. Meth.* A571 (2007) 687.
- [8] C. Szeles, W.C. Chalmers, S.C. Cameron, J.-O. Ndap, M. Bliss, K.G. Lynn, *SPIE Proc.* 4507 (2001) 57.
- [9] P. Rudolph, M. Neubert, M. Mühlberg, *J. Cryst. Growth* 128 (1993) 582.
- [10] P. Rudolph, A. Engel, I. Schentke, A. Grochochi, *J. Cryst. Growth* 147 (1995) 297.
- [11] R.S. Rai, S. Mahajan, S. McDevitt, C.J. Johnson, *J. Vac. Sci. Technol.* B9 (1996) 1892.
- [12] L. Li, F. Lu, K. Shah, M. Squillante, L. Cirinano, W. Yao, R.W. Olson, P. Luke, Y. Nemirovsky, A. Burger, G. Wright, R.B. James, *Nucl. Sci. Symp. Conf. Rec. IEEE* 4 (2001) 2396.
- [13] H. Chen, S.A. Awadalla, J. Mackenzie, R. Redden, G. Bindley, A.E. Bolotnikov, G.S. Camarda, G. Carini, R.B. James, *IEEE Trans. Nucl. Sci.* 54 (2007) 811.
- [14] H. Chen, S.A. Awadalla, K. Iniewski, P.H. Lu, F. Harris, J. Mackenzie, T. Hasanen, W. Chen, R. Redden, G. Bindley, I. Kuvvetli, C. Budtz-Jørgensen, P. Luke, M. Amman, J.S. Lee, A.E. Bolotnikov, G.S. Camarda, Y. Cui, A. Hossain, R.B. James, *J. Appl. Phys.* 103 (2008) 014903.
- [15] M.C. Duff, D.B. Hunter, A. Burger, M. Groza, V. Buliga, J.P. Bradley, G. Graham, Z. Dai, N. Teslich, D.R. Black, A. Lanzirotti, *J. Mater. Res.* 24 (2009) 1361.
- [16] L.M. Bartlett, C.M. Stahle, D. Palmer, L.M. Barbier, S.D. Barthelmy, F. Birsa, N. Grehrels, J.F. Krizmanic, P. Kurczynski, J. Odom, A.M. Parsons, C. Sappington, P. Shu, B.J. Teegarden, J. Trueller, *Proc. Soc. Photo-Opt. Instrum. Eng.* 2806 (1996) 616.
- [17] D.R. Rhiger, R.E. Kvaas, *J. Vac. Sci. Technol.* 21 (1982) 168.